Photon-counting CT for simultaneous imaging of multiple contrast agents in the abdomen: An *in vivo* study

Rolf Symons
Radiology Imaging Sciences, National Institutes of Health Clinical Center, Bethesda, MD, USA

Bernhard Krauss
Computed Tomography Division, Siemens Healthcare GmbH, Forchheim, Germany

Pooyan Sahbaee
Imaging and Therapy Systems, Siemens Medical Solutions Inc., Malvern, PA, USA

Tyler E. Cork, Manu N. Lakshmanan, David A. Bluemke, and Amir Pourmorteza[a)]
Radiology Imaging Sciences, National Institutes of Health Clinical Center, Bethesda, MD, USA

(Received 4 October 2016; revised 7 April 2017; accepted for publication 14 April 2017; published 20 August 2017)

Purpose: To demonstrate the feasibility of spectral imaging using photon-counting detector (PCD) x-ray computed tomography (CT) for simultaneous material decomposition of three contrast agents *in vivo* in a large animal model.
Methods: This Institutional Animal Care and Use Committee-approved study used a canine model. Bismuth subsalicylate was administered orally 24–72 h before imaging. PCD CT was performed during intravenous administration of 40–60 ml gadoterate meglumine; 3.5 min later, iopamidol 370 was injected intravenously. Renal PCD CT images were acquired every 2 s for 5–6 min to capture the wash-in and wash-out kinetics of the contrast agents. Least mean squares linear material decomposition was used to calculate the concentrations of contrast agents in the aorta, renal cortex, renal medulla and renal pelvis.
Results: Using reference vials with known concentrations of materials, we computed molar concentrations of the various contrast agents during each phase of CT scanning. Material concentration maps allowed simultaneous quantification of both arterial and delayed renal enhancement in a single CT acquisition. The accuracy of the material decomposition algorithm in a test phantom was -0.4 ± 2.2 mM, 0.3 ± 2.2 mM for iodine and gadolinium solutions, respectively. Peak contrast concentration of gadolinium and iodine in the aorta, renal cortex, and renal medulla were observed 16, 24, and 60 s after the start each injection, respectively.
Conclusion: Photon-counting spectral CT allowed simultaneous material decomposition of multiple contrast agents *in vivo*. Besides defining contrast agent concentrations, tissue enhancement at multiple phases was observed in a single CT acquisition, potentially obviating the need for multiphase CT scans and thus reducing radiation dose. © *2017 American Association of Physicists in Medicine* [https://doi.org/10.1002/mp.12301]

Key words: contrast agents, k-edge imaging, material decomposition, multi-contrast, photon-counting CT, spectral CT

1. INTRODUCTION

Photon-counting detectors combined with CT have the potential to provide improvements on the capabilities of DECT by resolving the incident x-ray energy spectrum into multiple energy bins.[1–3] Whereas current spectral CT scanners identify two x-ray spectra, photon-counting detector (PCD) CT has been implemented in prototype form with four energy bins.[4] This would enable simultaneous material classification of multiple contrast agents.

A potential use of PCD CT may be for quantitative abdominal imaging.[5,6] For example, accurate diagnosis and staging of renal abnormalities typically requires an unenhanced acquisition and up to three contrast-enhanced acquisitions (corticomedullary, nephrogenic, and excretory phases), resulting in high radiation doses of 15–30 mSv.[7,8] Multiple split-bolus techniques with separate contrast agent bolus injections have been developed to acquire nephrogenic and excretory images in 1 acquisition, reducing the number of acquisitions and hence radiation dose.[9] In addition, dual-energy CT (DECT) can be used to decompose images into two basis materials e.g., one contrast material versus soft tissue and has been used as an alternative method to reduce radiation dose in multiphase abdominal CT protocols by calculation of virtual noncontrast images based on the energy-dependent properties of iodine contrast agents.[10,11]

Previous studies in phantoms and animal models have shown the potential of photon-counting CT for simultaneous multicontrast imaging *ex vivo*.[1,12,13] The purpose of this study was to determine the potential of photon-counting CT for *in vivo*, simultaneous differentiation of three contrast agents (intravenous gadolinium and iodine and oral bismuth). For this purpose, we used a large animal

model and a novel human prototype photon-counting CT scanner.

2. MATERIALS AND METHODS

2.A. Animal model

In this Institutional Animal Care and Use Committee-approved (IACUC) study (DRD 14-05), we studied three adult male mongrel dogs (24–30 kg). General anesthesia was induced by intramuscular injection of a combination of ketamine (5.5 mg/kg), acepromazine (0.05–0.11 mg/kg), and torbugesic (0.2 mg/kg) with atropine (0.04 mg/kg) as a separate injection and intravenous meloxicam (0.2 mg/kg) for analgesia. After endotracheal intubation, anesthesia was maintained via inhalation with isoflurane (1–2%) with oxygen at a total flow rate of 2 L/min during imaging. Automatic mechanical ventilation with a tidal volume of 15 mL/kg and a breathing frequency of 15 breaths/min was performed with continuous recording of a pulse oximeter and a 4-lead electrocardiogram. The animal model was part of a larger study and was not created solely for the purpose of this experiment.

2.B. Photon-counting CT imaging system

The research whole-body PCD CT system is based on a second generation dual-source CT scanner (SOMATOM Definition Flash, Siemens Healthcare, Forchheim, Germany) in which one of the conventional energy-integrating detectors (EIDs) is replaced by a cadmium telluride-based PCD. Up to four energy thresholds between 20 and 90 keV can be defined for the PCD at 1 keV increments (2 "low" thresholds between 20 and 50 keV, and 2 "high" thresholds between 50 and 90 keV). Tube voltages can be set at 80 kVp, 100 kVp, 120 kVp, and 140 kVp with tube current values between 25 mA and 550 mA (in steps of 1 mA). Rotation times are fixed at 0.5 and 1.0 s. Detailed information of this prototype scanner has been previously described.[4]

2.C. Photon-counting CT scan protocol

Bismuth subsalicylate (60 mg, Pepto-bismol, Procter & Gamble, Cincinnati, OH, USA) was administered orally 24–72 h prior to scanning. PCD CT was performed during intravenous administration of gadolinium-based contrast (40–0 mL, 3 mL/s, Dotarem, Guerbet, Roissy, France) followed after 3–4 min by iodine-based contrast (20 mL, 3 mL/s, Isovue 370, Bracco Diagnostics, Princeton, NJ, USA). CT images were acquired every 2 s at the level of the left renal pelvis to visualize the kinetics of contrast enhancement and excretion in the kidney for both contrast agents. At the 2-min time point, there was a 1 min pause in imaging for tube cooling; scanning then continued for a total of 5–6 min (Fig. 1).

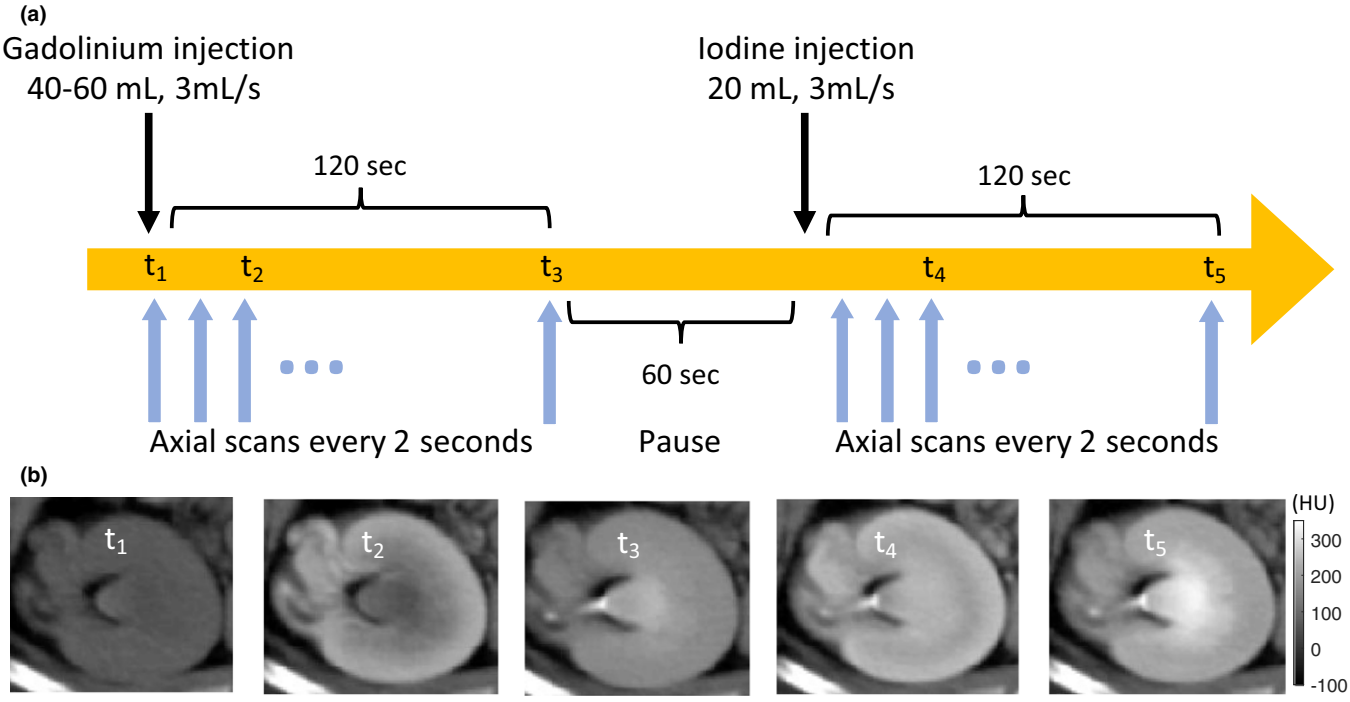

FIG. 1. (a) Photon-counting scan protocol: First, gadolinium-based contrast (40–60 mL, 3 mL/s) was injected, followed by axial CT scans every 2 s at the level of the left renal pelvis. After 2 min, there was a 1 min pause in imaging to avoid overheating of the x-ray tube. Next, iodine-based contrast (20 mL, 3 mL/s) was injected, followed by axial CT scans every 2 s for 2 min. (b) Example grayscale photon-counting images at different time points: t_1 = precontrast; t_2 = corticomedullary gadolinium enhancement; t_3 = excretory gadolinium enhancement; t_4 = corticomedullary iodine enhancement, excretory gadolinium enhancement; t_5 = excretory iodine and gadolinium enhancement. Without prior information, it is not possible to differentiate the two contrast agents on these grayscale images. [Color figure can be viewed at wileyonlinelibrary.com]

The gadolinium- and iodine-based contrast agents were injected sequentially to visualize different phases of renal enhancement at the same time point in a single CT acquisition (e.g., corticomedullary phase iodine enhancement and nephrogenic gadolinium enhancement). With a high k-edge energy of 90 keV, the oral bismuth agent was used to demonstrate the potential of photon-counting CT to differentiate more than three contrast agents *in vivo*. The iodine concentration of 0.7–0.8 mL/kg of body weight was within the concentration limits of common clinical protocols (0.7–2.0 mL/kg of body weight for an average 70 kg patient).[14] The gadolinium-based contrast agent concentration of 1.7–2.0 mL/kg of body weight was significantly higher than the 0.2 mL/kg concentration currently used in MRI. Previous CT studies have shown that higher gadolinium concentrations (up to 0.8 mL/kg) are necessary to achieve equivalent x-ray attenuation doses to iodine-based contrast agents.[15,16] In this proof of concept study, the primary objective was to demonstrate the feasibility of separating two mixed contrast agents *in vivo*. Consequently, we did not examine the lowest possible contrast dose and used a high gadolinium concentration to allow for real-time visualization of renal gadolinium enhancement (prior to material decomposition) and appropriate timing of the subsequent iodine injection.

Scan parameters were 140 kVp tube voltage, 300 mAs tube current, 0.5 s rotation time and energy thresholds of 25, 50, 75, and 90 keV. These settings resulted in four energy bins (25–50 keV, 50–75 keV, 75–90 keV, and 90–140 keV). After 6 min, an additional delayed CT acquisition was performed. Figure 2 shows the shape of the effective x-ray spectrum detected in the PCD energy bins after passing through 20 cm of water and is calculated using a simulation toolbox provided by the manufacturer. Spectral separation between bins is not perfect due to intrinsic physical processes within the detector e.g., k-escape and charge sharing.[3] The thresholds were chosen based on previous phantom experiments demonstrating good differentiation of iodine-, gadolinium-, and bismuth-based contrast agents. Images were reconstructed with a quantitative soft tissue kernel (D30f), slice thickness of 1 mm, and increment of 1 mm. By combining all four energy bins, PCD images which contain all detected photons can be reconstructed. The quality of these PCD images has been shown to be at

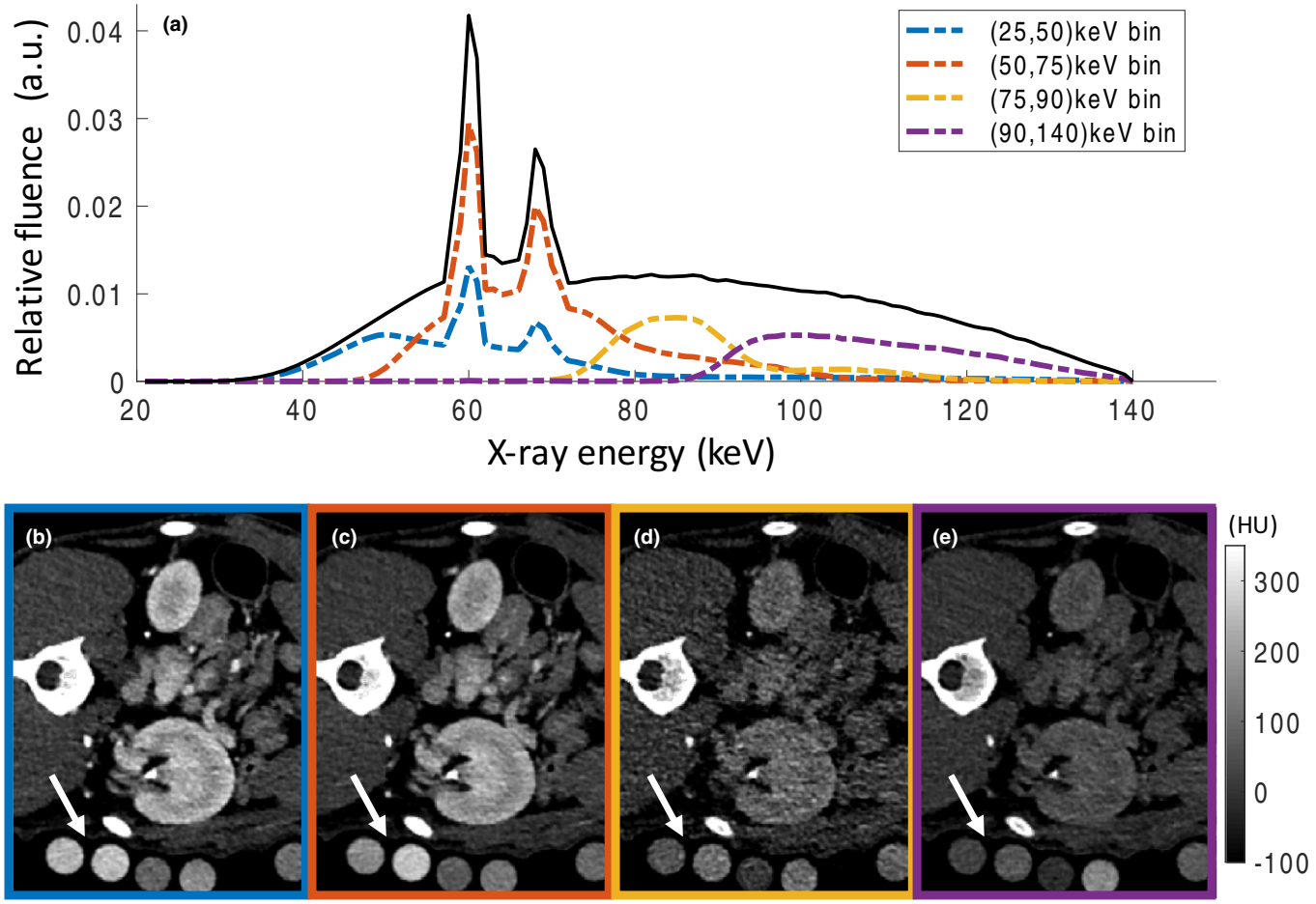

FIG. 2. (a) Shape of the x-ray spectrum detected in the photon-counting detector (PCD) considering the detector response function. (b–e) Axial PCD CT from the four bins [(25,50), (50,75), (75,90), and (90,140)] at the level of the left renal pelvis. Calibration vials with known concentrations of iodine, gadolinium, and bismuth (arrows) are placed within the field-of-view (FOV) and used in the linear material decomposition algorithm. Based on the conventional grayscale images, differentiation between the different contrast agents is impossible without prior knowledge.

least similar to conventional EID images in phantoms and *in vivo*.[17,18]

2.D. Image-based material decomposition

Image-based material decomposition has been explicitly validated for clinical dual-energy CT[19–21] and experimental multienergy photon-counting CT scans[22] and avoids the more complicated projection-based processing,[23] which requires extensive calibrations and access to the proprietary projection data. In the proposed approach, only beam hardening by water is taken into account, but not beam hardening by the contrast agents. As a consequence, it is not necessary to specify the x-ray attenuation of the base materials as a function of energy or to choose specific basis functions, such as the attenuation curves of water or iodine or even more sophisticated entities.[24]

The image-based material decomposition algorithm is based on mass conservation; image voxels containing multiple materials, such as a mixture of blood, gadolinium, and iodine, have CT numbers that equal a linear combination of the CT numbers of the mixed materials. Therefore, material decomposition can be framed as a system of linear equations; for one voxel, we can write

$$[CT]_{4\times1} = [M]_{4\times4}[\rho]_{4\times1}, \quad (1)$$

where CT is a vector of CT numbers of the four energy bins/thresholds of one voxel, ρ is a vector of concentration of each of the four basis materials, and matrix M encodes the contribution of each basis material to the attenuation measured in each energy bin.

Matrix M is determined through calibration. The calibration may be performed by scanning phantoms with vials of known concentrations and mixtures of the basis materials at the same tube voltage and detector energy threshold settings, or by placing the calibration vials under the animals during the scan [Figs. 2(b)–2(e)]. The M matrix is calculated by least square fitting of the known material concentrations and the measured CT numbers. We placed calibration vials with gadolinium (40 mM), iodine (10 mM), bismuth (48.2 mM), and an aqueous solution of ferrous sulfate ($FeSO_4$, 10 mM), which closely represents the spectral properties of soft tissue e.g., blood, liver, and kidney parenchyma underneath the animal within the FOV during the scanning.[21] The gadolinium and iodine concentrations were chosen such that they produce attenuations close to the CT numbers of contrast-enhanced kidney in clinical renal CT scans.

As the local contrast agent concentrations are the clinically interesting quantities to be extracted and there are exactly four measured spectral channels for the same number of base materials, there are no free parameters to improve image noise after conventional base material decomposition without losing clinical interpretability. We only have reduced noise to an acceptable level by adding information from neighboring voxels using the basic smooth 5 × 5 convolution filter in Osirix (Pixmeo, Geneva, Switzerland), so that spatial resolution of the results is also reduced. As a consequence of this approach, the mathematical complexity of base material decomposition is reduced to a minimum, while being sufficient for the purpose of this study.

In addition to the animal studies, we scanned a calibration phantom made of a circular water phantom (20 cm diameter) with vials of multiple concentrations and mixtures of iodine and gadolinium in order to test the performance of the algorithm. The phantom scan and reconstruction parameters were similar to those of the animal scans.

A separate 3-material decomposition was performed, with gadolinium, ferrous sulfate, and calcium (hydroxyapatite) as basis materials, in order to highlight dense calcifications and bones. It should be noted that linear attenuations of iodine and calcium are similar in diagnostic CT range of energies and may not be distinguishable under this decomposition. Therefore, an additional constraint (Bin 1 > 500 HU, chosen heuristically above the CT numbers of iodine in this study) was used to create a bone mask.

3. RESULTS

Figure 3 shows the animal PCD CT scan setup with calibration vials containing known concentrations of iodine-, gadolinium-, and bismuth-based contrast agents under the animal at the level of the left kidney. The three contrast materials cannot be differentiated on the grayscale images and the radiopacity of the aorta and kidney of the animals could be attributed to any combination of the contrast materials. Conversely, the material concentration maps from the PCD CT images allowed clear differentiation of the contrast agents in the calibration vials and *in vivo*.

We tested the accuracy of the material decomposition algorithm in a water phantom containing vials of known concentrations and mixtures of the basis materials. The M matrix was estimated using the spectral attenuation values of vials of iodine, gadolinium, bismuth, and ferrous sulfate at 10 mM, 20 mM, 48.2 mM, and 10 mM, respectively and a vial containing 10 mM of iodine and 5 mM of gadolinium. The accuracy was tested on vials with different concentrations of gadolinium (5, 10, 20 mM), iodine (5, 10, 20 mM), two mixtures of gadolinium and iodine (10:5 mM and 5:10 mM), as well as the calibration vials.

The mean ± SD of the difference between the estimated and true concentrations of the test vials was −0.4 ± 2.2 mM, 0.3 ± 2.2 mM, 0.0 ± 2.4 mM, and −0.0 ± 1.4 mM for iodine, gadolinium, bismuth, and ferrous sulfate vials in the test phantom, respectively, showing very small bias from the truth. The error was 1.4 ± 0.2 mM and 0.9 ± 0.5 mM for the gadolinium (40 mM) and iodine (10 mM) vials placed under the three animals, respectively, showing good reproducibility between the three scans.

In vivo grayscale images at multiple time points after administration, the three contrast agents show high-attenuation contrast agents in the small bowel lumen, renal cortex, and renal excretory system [Figs. 4(a) and 4(b)]. As we expected, there was little or no difference in grayscale appearance of the contrast agents.

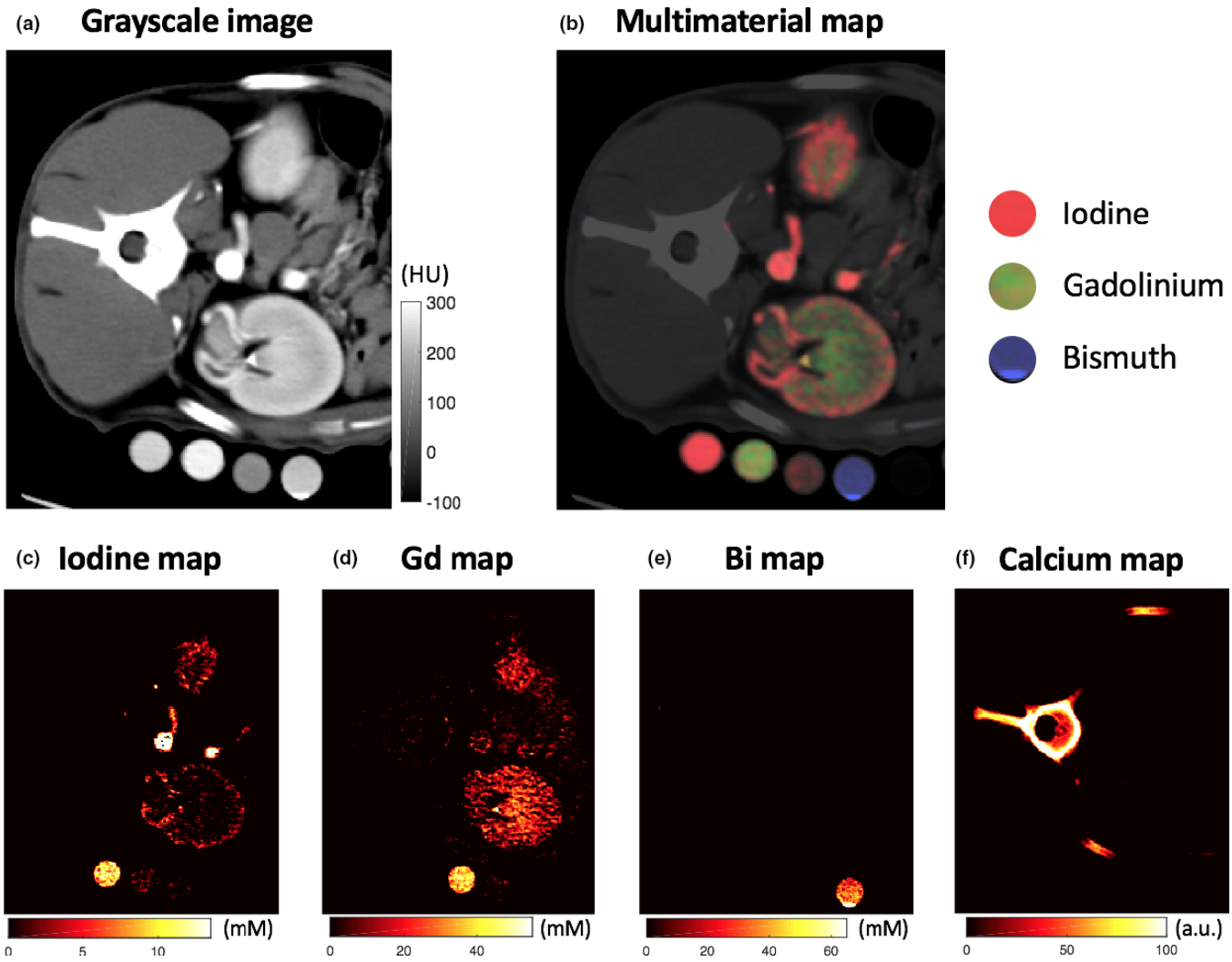

FIG. 3. (a) Grayscale photon-counting detector (PCD) image reconstructed from all detected photons regardless of their detected energy at the level of the left pelvis demonstrates the dense contrast material in the calibration vials, abdominal aorta, and kidney. No differentiation is possible between the different contrast agents in single energy CT. (b) PCD multimaterial map differentiates the iodine (red), gadolinium (green), and bismuth (blue) contrast agents. Iodine (c), gadolinium (d), bismuth (e), and calcium (f) material map reveals which calibration vials contain which contrast agents with arterial corticomedullary iodine enhancement and venous nephrogenic/excretory enhancement within the kidney. mM = millimolar.

Time-attenuation curves for gadolinium and iodine in the regions-of-interest (ROIs) in the aorta, renal cortex, renal medulla, and renal pelvis were significantly different making contrast agent separation possible [Figs. 4(c) and 4(d)]. A video of the dynamic dual-contrast kinetics in the kidney of another test subject is available in the *Online appendix*. Peak contrast concentration in the aorta, renal cortex, and renal medulla were observed approximately 16, 24, and 60 s after each injection, respectively. A second, smaller peak in contrast concentration in the aorta and renal cortex due to contrast reperfusion could be detected 20 s after the first-pass enhancement. Contrast agent excretion in the renal pelvis started 60 s after injection and reached a plateau after 2–3 min for both gadolinium and iodine. A mixture of iodine and gadolinium could be detected in the bladder after renal excretion (Fig. 5). Bismuth, which was used as an enteric contrast agent, was easily differentiable from the other two contrast agents on the material concentration maps.

4. DISCUSSION

This proof of principle study is the first to demonstrate the *in vivo* use of spectral photon-counting CT for the differentiation of three contrast agents in a large animal model. The proposed method allowed successful estimation of the concentration of different contrast agents from a mixture both *in vitro* and *in vivo*.

A potential advantage of performing split-bolus dual-contrast photon-counting CT for multiphase kidney imaging is the reduction in radiation dose. With conventional energy-integrating detector (EID) CT, multiphase acquisitions are typically used (either 3 or 4 phase acquisition). Thus, the use of spectral CT alone, such as dual-energy CT, can result in significant radiation dose reduction using "virtual noncontrast" imaging. However, with conventional CT, we have not previously had the possibility of differentiating multiple contrast agents. As a result, rather than use high-attenuation

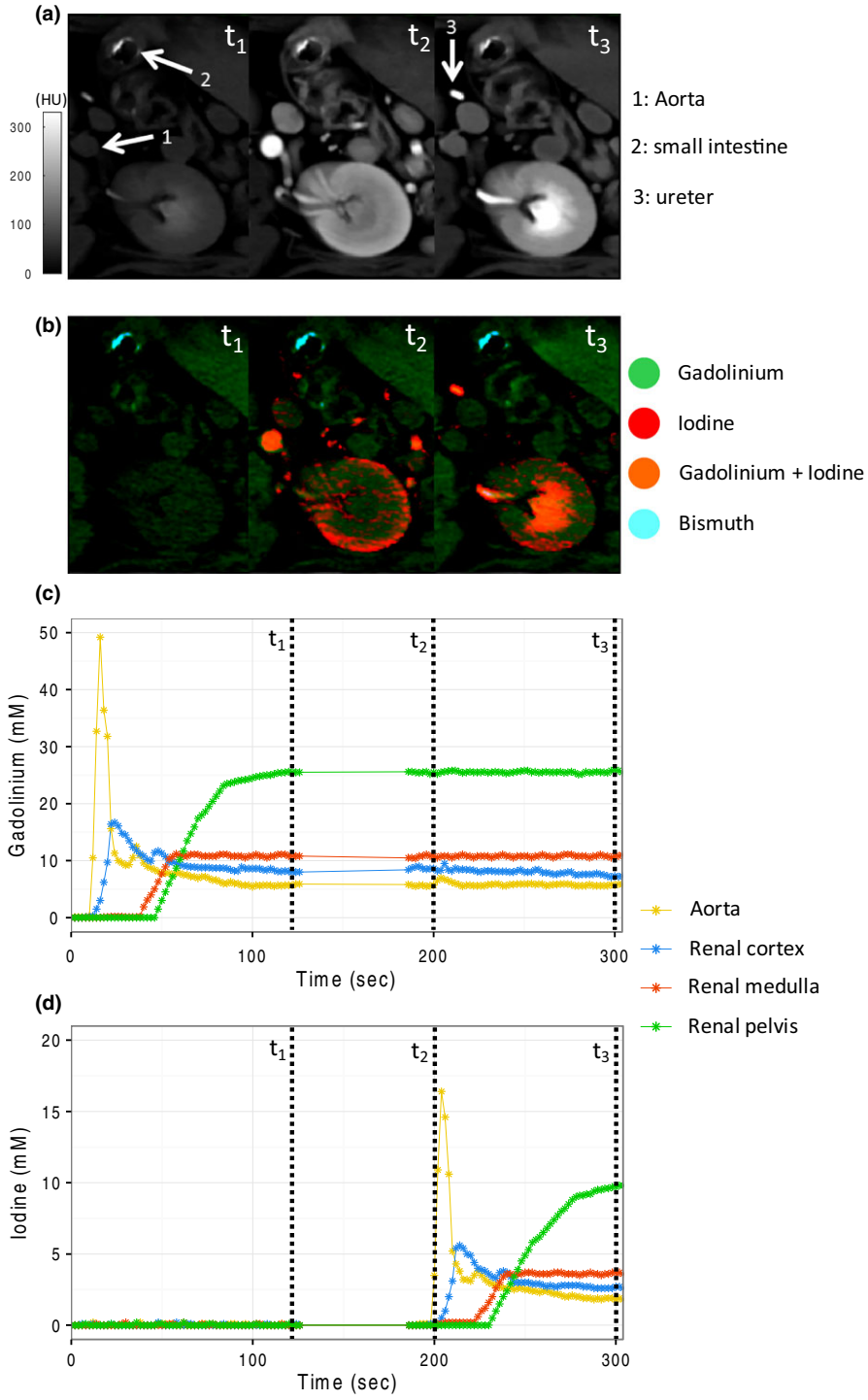

FIG. 4. Grayscale images (a) and multimaterial maps (b) at three time points during the scan protocol: t_1 = gadolinium excretory phase (120 s after gadolinium injection); t_2 = iodine arterial phase, gadolinium excretory phase (200 s after gadolinium injection, 20 s after iodine injection); t_3 = iodine and gadolinium excretory phase (300 s after gadolinium injection, 120 s after iodine injection). Differentiation between the three contrast agents is possible on the multimaterial maps. Time-concentration curves for gadolinium (c) and iodine (d) in the aorta, renal cortex, renal medulla, and renal pelvis show clear differentiation of the contrast materials.

contrast agents for the bowel, water or air is more frequently used with current generation CT in order to separate vascular from nonvascular bowel. It appears possible that photon-counting CT may encourage development of alternative and potentially more specific or sophisticated CT contrast agents.[25] In addition, multicontrast imaging with photon CT has the advantage of perfect coregistration of all material maps. This is particularly important for moving structures due to breathing or bowel peristalsis.

In additional to visual assessment, PCD material concentration maps are quantitative. With conventional EID CT, overlap in HU values between different materials (i.e., iodine

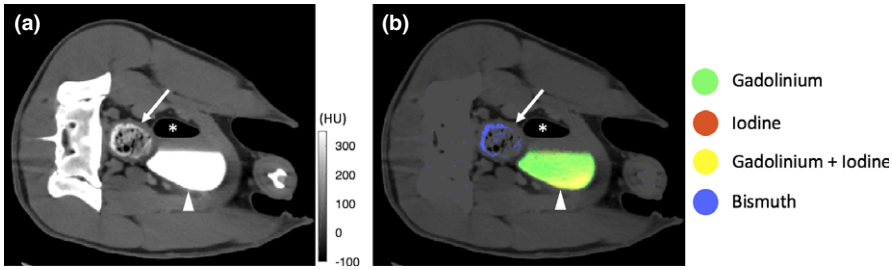

FIG. 5. Grayscale images (a) and multimaterial maps (b) at the level of the bladder. There is a mixture of iodine and gadolinium in the dependent portion of the bladder after renal excretion (arrowhead). The orally ingested bismuth in the colon is clearly distinguishable from the iodine/gadolinium mixture in the bladder (arrow). The multimaterial map allows for differentiation between the contrast materials (* air in the bladder after bladder catheterization).

contrast material vs calcified plaques) might hinder accurate diagnosis. Spectral imaging with PCDs like the one used in this study may quantify the composition of each image voxel into two or more known base materials. This spectral information can be used for the *in vivo* characterization of kidney stones or the differentiation of enhancing lesions versus spontaneously hyperdense cysts with high proteinaceous or hemorrhagic content (iodine vs iron or protein).[26,27] Differentiation of enteric and intravascular contrast materials may be useful in trauma imaging, where identification of the source of free intra-abdominal contrast medium enables diagnosis of hemorrhage versus bowel perforation.[28] Muenzel et al. demonstrated the potential of photon-counting CT for differentiation of gadolinium-enhanced polyps and iodine-tagged fecal material in a colon phantom.[29] Here, we demonstrated the possibility of using bismuth *in vivo* as an enteric contrast material to complement iodine and gadolinium intravascular contrast.

Our study had limitations; iodine-based contrast agents are the only FDA-approved agents for human CT imaging, rendering dual- or multicontrast CT in humans highly unlikely at this moment. We used bismuth subsalicylate due to its off-the-shelf availability and relatively favorable toxicity profile. However, due to its low solubility in water and the potential of salicylate toxicity, bismuth subsalicylate is of limited use as a contrast agent for imaging in human subjects.[30] Our study demonstrates the potential of spectral CT for multicontrast differentiation and we hope this will intensify the ongoing research and development of new CT contrast agents.[25] The threshold settings, reconstruction kernels and material decomposition method used in this study remain novel and thus are likely not necessarily optimal. We used an image-based material decomposition method. Photon-counting CT is less susceptible to beam hardening due to the narrower spectrum in each energy bin compared to single-kV imaging, which reduces error during log normalization.[31] However, residual beam hardening effects may be a potential source of error within our material decomposition technique.[3,32] Finally, we did not apply any noise-reduction algorithms when generating the material maps, since image noise was sufficiently low in the original images. However, it has been shown that for DECT, the linear material decomposition leads to large and anticorrelated noise in the material maps.[33,34] Similarly, base material images from multienergy imaging e.g., spectral photon-counting scans, suffer from increased image noise. Although algorithms have been developed for dual-energy CT to cope with this challenge, the application of these methods to multienergy CT is beyond the scope of this article.[35]

In conclusion, this study shows the feasibility of using photon-counting CT with four energy thresholds to differentiate three k-edge contrast agents *in vivo*. In combination with advanced multienergy noise-reduction algorithms split-bolus multicontrast photon-counting CT imaging has the potential to dramatically reduce the radiation dose of multiphase CT imaging protocols while providing inherently registered spectral images and material concentration maps.

ACKNOWLEDGMENTS

This study was supported by the NIH intramural research program (ZIACL090019; ZIAEB000072), and a collaborative research agreement with Siemens Healtcare GmbH (Forchheim, Germany). The authors wish to thank: Dr. Kelly A. Rice (National Institutes of Health, Division of Veterinary Resources) for her help with creating and handling the animal model; Drs. André Henning, Martin Sedlmair, Friederike Schöck (Siemens Healthcare GmbH, Forchheim, Germany) for building and maintaining the prototype scanner and reconstruction pipeline; Drs. Bernhard Schmidt and Tristan Nowak (Siemens Healthcare GmbH) for helpful discussions regarding material decomposition and multicolor visualization; Drs. Steffen Kappler and Stefan Ulzheimer (Siemens Healthcare GmbH) for providing the photon-counting x-ray spectral response simulation toolbox and for insightful discussions regarding the CT physics of photon-counting detectors and image formation and Dr. Ulzheimer for overseeing and supporting the NIH-Siemens cooperative research and development agreement on photon-counting CT research.

CONFLICTS OF INTEREST

This study was supported by a research agreement with Siemens Healthcare GmbH (Forchheim, Germany). Authors who are not employees of or consultants for Siemens had

control of data inclusion and analysis that might present a conflict of interest for the authors who are employed by Siemens.

[a]Author to whom correspondence should be addressed. Electronic mail: amir.pourmorteza@nih.gov.

REFERENCES

1. Schlomka JP, Roessl E, Dorscheid R, et al. Experimental feasibility of multi-energy photon-counting K-edge imaging in pre-clinical computed tomography. *Phys Med Biol*. 2008;53:4031.
2. Iwanczyk JS, Nygard E, Meirav O, et al. Photon counting energy dispersive detector arrays for x-ray imaging. *IEEE Trans Nucl Sci*. 2009;56: 535–542.
3. Taguchi K, Iwanczyk JS. Vision 20/20: single photon counting x-ray detectors in medical imaging. *Med Phys*. 2013;40:100901.
4. Kappler S, Henning A, Kreisler B, Schoeck F, Stierstorfer K, Flohr T. Photon counting CT at elevated X-ray tube currents: contrast stability, image noise and multi-energy performance; 2014, p. 90331C–90331C–8.
5. Szolar DH, Kammerhuber F, Altziebler S, et al. Multiphasic helical CT of the kidney: increased conspicuity for detection and characterization of small (< 3-cm) renal masses. *Radiology*. 1997;202:211–217.
6. Israel GM, Bosniak MA. How I do it: evaluating renal masses. *Radiology*. 2005;236:441–450.
7. Nawfel RD, Judy PF, Schleipman AR, Silverman SG. Patient radiation dose at CT urography and conventional urography. *Radiology*. 2004;232:126–132.
8. Dillman JR, Caoili EM, Cohan RH. Multi-detector CT urography: a one-stop renal and urinary tract imaging modality. *Abdom Imaging*. 2007;32:519–529.
9. Kekelidze M, Dwarkasing RS, Dijkshoorn ML, Sikorska K, Verhagen PCMS, Krestin GP. Kidney and urinary tract imaging: triple-bolus multidetector CT urography as a one-stop shop—protocol design, opacification, and image quality analysis. *Radiology*. 2010;255:508–516.
10. Graser A, Johnson TRC, Hecht EM, et al. Dual-energy CT in patients suspected of having renal masses: can virtual nonenhanced images replace true nonenhanced images? *Radiology*. 2009;252:433–440.
11. Toepker M, Kuehas F, Kienzl D, et al. Dual energy computerized tomography with a split bolus—a 1-stop shop for patients with suspected urinary stones? *J Urol*. 2014;191:792–797.
12. Cormode DP, Roessl E, Thran A, et al. Atherosclerotic plaque composition: analysis with multicolor CT and targeted gold nanoparticles. *Radiology*. 2010;256:774–782.
13. Symons R, Cork TE, Lakshmanan MN, et al. Dual-contrast agent photon-counting computed tomography of the heart: initial experience. *Int J Cardiovasc Imaging*. 2017;March: 1–9.
14. Bae KT. Intravenous contrast medium administration and scan timing at CT: considerations and approaches. *Radiology*. 2010;256:32–61.
15. Gierada DS, Bae KT. Gadolinium as a CT contrast agent: assessment in a porcine model. *Radiology*. 1999;210:829–834.
16. Remy-Jardin M, Dequiedt P, Ertzbischoff O, et al. Safety and effectiveness of gadolinium-enhanced multi-detector row spiral CT angiography of the chest: preliminary results in 37 patients with contraindications to iodinated contrast agents. *Radiology*. 2005;235:819–826.
17. Symons R, Cork TE, Sahbaee P, et al. Low-dose lung cancer screening with photon-counting CT: a feasibility study. *Phys Med Biol*. 2016;62:202.
18. Pourmorteza A, Symons R, Sandfort V, et al. Abdominal imaging with contrast-enhanced photon-counting CT: first human experience. *Radiology*. 2016;279:239–245.
19. Toepker M, Moritz T, Krauss B, et al. Virtual non-contrast in second-generation, dual-energy computed tomography: reliability of attenuation values. *Eur J Radiol*. 2012;81:e398–e405.
20. Brooks RA. A quantitative theory of the Hounsfield unit and its application to dual energy scanning. *J Comput Assist Tomogr*. 1977;1: 487–493.
21. Johnson TRC, Krauss B, Sedlmair M, et al. Material differentiation by dual energy CT: initial experience. *Eur Radiol*. 2007;17:1510–1517.
22. Li Z, Leng S, Yu L, Yu Z, McCollough CH. Image-based material decomposition with a general volume constraint for photon-counting CT. In: *SPIE Med. Imaging*. San Diego, CA: International Society for Optics and Photonics; 2015:94120T.
23. Alvarez RE, Macovski A. Energy-selective reconstructions in x-ray computerised tomography. *Phys Med Biol*. 1976;21:733.
24. Xing Y, Li Y, Shen L. A general adaptive decomposition method for multi-energy spectral CT. In: *Nucl Sci Symp Med Imaging Conf (NSS/MIC)*. Seoul: IEEE; 2013:1–4.
25. Yeh BM, FitzGerald PF, Edic PM, et al. Opportunities for new CT contrast agents to maximize the diagnostic potential of emerging spectral CT technologies. *Adv Drug Deliv Rev* 2016 [Epub ahead of print].
26. Primak AN, Fletcher JG, Vrtiska TJ, et al. Noninvasive differentiation of uric acid versus non–uric acid kidney stones using dual-energy CT. *Acad Radiol*. 2007;14:1441–1447.
27. Boll DT, Patil NA, Paulson EK, et al. Focal cystic high-attenuation lesions: characterization in renal phantom by using photon-counting spectral CT—improved differentiation of lesion composition. *Radiology*. 2009;254:270–276.
28. Mongan J, Rathnayake S, Fu Y, Gao D-W, Yeh BM. Extravasated contrast material in penetrating abdominopelvic trauma: dual-contrast dual-energy CT for improved diagnosis—preliminary results in an animal model. *Radiology*. 2013;268:738–742.
29. Muenzel D, Bar-Ness D, Roessl E, et al. Spectral photon-counting CT: initial experience with dual-contrast agent K-edge colonography. *Radiology*. 2016:160890 [Epub ahead of print].
30. Sainsbury SJ. Fatal salicylate toxicity from bismuth subsalicylate. *West J Med*. 1991;155:637.
31. Shikhaliev PM. Beam hardening artefacts in computed tomography with photon counting, charge integrating and energy weighting detectors: a simulation study. *Phys Med Biol*. 2005;50:5813.
32. Zou Y, Silver MD. Analysis of fast kV-switching in dual energy CT using a pre-reconstruction decomposition technique. In: *Med. Imaging*. Dresden: International Society for Optics and Photonics; 2008: 691313.
33. Kalender WA, Klotz E, Kostaridou L. An algorithm for noise suppression in dual energy CT material density images. *IEEE Trans Med Imaging*. 1988;7:218–224.
34. Petrongolo M, Dong X, Zhu L. A general framework of noise suppression in material decomposition for dual-energy CT. *Med Phys*. 2015;42:4848–4862.
35. Grant KL, Flohr TG, Krauss B, Sedlmair M, Thomas C, Schmidt B. Assessment of an advanced image-based technique to calculate virtual monoenergetic computed tomographic images from a dual-energy examination to improve contrast-to-noise ratio in examinations using iodinated contrast media. *Invest Radiol*. 2014;49:586–592.

SUPPORTING INFORMATION

Additional Supporting Information may be found online in the supporting information tab for this article.

Video S1. Dynamic visualization of dual-contrast kinetics in the kidney.